Integral bridge abutment with composite dowels: structural scheme and failure patterns

Zhihua Xiong, Di Di*, Hui Wang, Zhenhua Pan
College of Water Resources and Architectural Engineering, Northwest A&F University, Yangling, China
xiongzhihua_2013@126.com, http://orcid.org/0000-0001-8796-1004
2022055844@nwafu.edu.cn, https://orcid.org/0009-0006-7465-966X
18112096768@nwafu.edu.cn, 2022050880@nwafu.edu.cn

Markus Feldmann
Institute of Steel Construction, RWTH Aachen University, Aachen, Germany
feldmann@stb.rwth-aachen.de

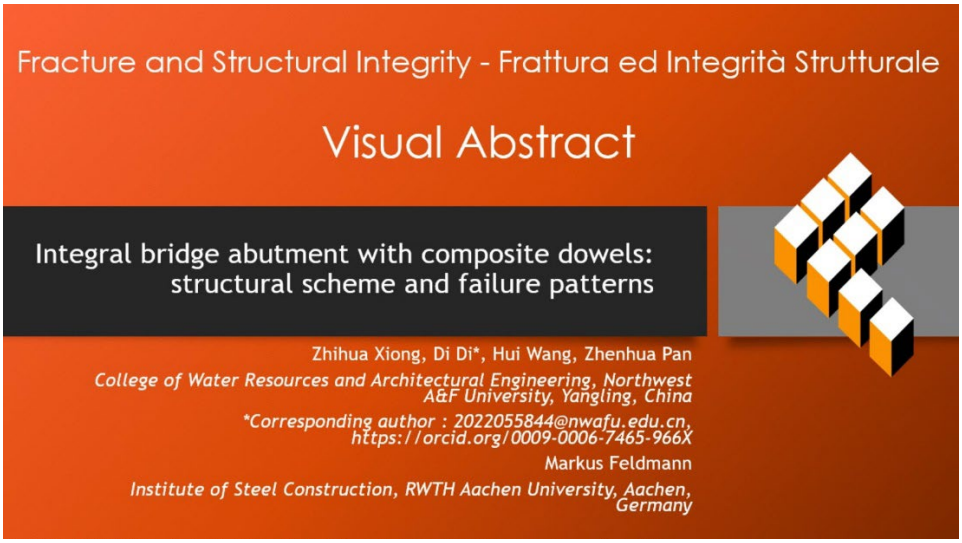

Citation: Xiong, Z, Di, D., Wang, H., Pan, Z, Feldmann, M., Integral bridge abutment with composite dowels: structural scheme and failure patterns, Fracture and Structural Integrity, 73 (2025) 267-284.

Received: 24.03.2025
Accepted: 13.06.2025
Published: 19.06.2025
Issue: 07.2025

KEYWORDS. Integral abutment, Composite dowels, Composite bridge, Girder-abutment joint, Jointless bridge.

INTRODUCTION

Integral bridges offer significant advantages over traditional bridges, including reduced construction costs by eliminating expansion joints and associated replacement. Additionally, they enhance bridge durability and safety, lower maintenance expenses, and significantly reduce lifecycle costs. However, the long-term shrinkage and creep of the concrete deck is inconsistent with the deformation of the steel girder, resulting in cumulative displacement at the abutment and even causing fatigue of the connector. At the meantime, the action of traffic load and temperature cycling also enhance the possibility of crack and fatigue of traditional connectors.

Integral bridges are generally categorized into three types: fully Integral Abutment Bridges (IABs), semi-integral abutment bridges, and extended deck slab bridges [1]. The economic and performance benefits of integral bridges are particularly

notable [2]. In the United States, at least 27 states have recognized the cost-effectiveness of jointless bridges [3], which provide improved seismic resistance and superior performance under extreme conditions due to their enhanced structural redundancy. Seismic fragility curves and evaluations for the hybrid concrete-steel frame were reported in [4].

H-shaped steel piles are widely used in IABs due to their flexibility, high strength, and ability to accommodate horizontal deformation. Arsoy et al. [5] demonstrated that H-shaped steel piles are the optimal choice for IABs. In terms of soil-structure interactions of IABs under seismic action, parametric studies indicated that low friction and dilatancy angles in granular fill resulted in unfavorable settlement patterns [6]. Shaking table tests demonstrated that compressible inclusions between the abutment and backfill effectively reduce seismic accelerations transmitted to the bridge deck and mitigate settlements [7].

The girder-abutment joint is a critical component of composite girder integral bridges. In steel-concrete composite girders, shear connectors are essential for transmitting shear forces and preventing relative slip at the steel-concrete interface. This ensures effective composite action between the two materials. Kim et al. [8] investigated the bearing capacity of joints, demonstrating that installing welded nail connectors and stiffener connectors enhances joint stiffness, bearing capacity, and crack resistance.

Conventional shear connectors, such as stud connectors and perfobond strip connectors, are widely employed in steel-concrete composite girders. However, perfobond connectors encounter challenges related to rebar penetration. In contrast, composite dowels overcome these limitations by eliminating the need for specialized welding and delivering robust performance even with lower-strength materials [9], which stimulates this work using the composite dowels as connectors. With regarding to the fatigue performance of composite dowels, we [10-11] analyzed composite dowels crack propagation under flexural/pure shear, revealing the relationships between stress intensity factor and crack length.

The European Design Manual for Integral Composite Girder Bridges [12] proposes a joint configuration as shown in Fig.1(a) wherein steel girders are directly placed on steel piles. This design eliminates batch casting requirements, transmits shear forces via weld studs, and transfers compressive forces to the bridge abutment through a bottom flange bearing plate. Ashiduka et al. [13] introduced an alternative joint design as shown in Fig.1(b), utilizing direct holes in the girder's flange and web to accommodate perforated steel bars. Riches et al. [14] proposed a configuration as shown in Fig.1(c) incorporating a bottom flange end plate to disperse concentrated loads, with tensile forces transmitted by steel reinforcement. The Japan Road Research Laboratory [15] conducted experimental and numerical studies on steel-concrete composite girder joints as shown in Fig.1(d), analyzing component-level load distribution. Briseghella et al. [16]] developed a design as shown in Fig.1(e) experimentally validated for hysteretic behavior, employing headless weld studs to transfer vertical shear forces, while tensile and compressive forces are transmitted through deck reinforcement and a bearing plate. Despite their merits, these configurations face practical challenges, including stud welding complexities, rebar penetration issues, concrete casting dead zones, and welding fatigue. To address these limitations, this study proposes a novel integral bridge abutment incorporating composite dowels girders as demonstrated in Fig 1(f), which is elaborated in the following sections.

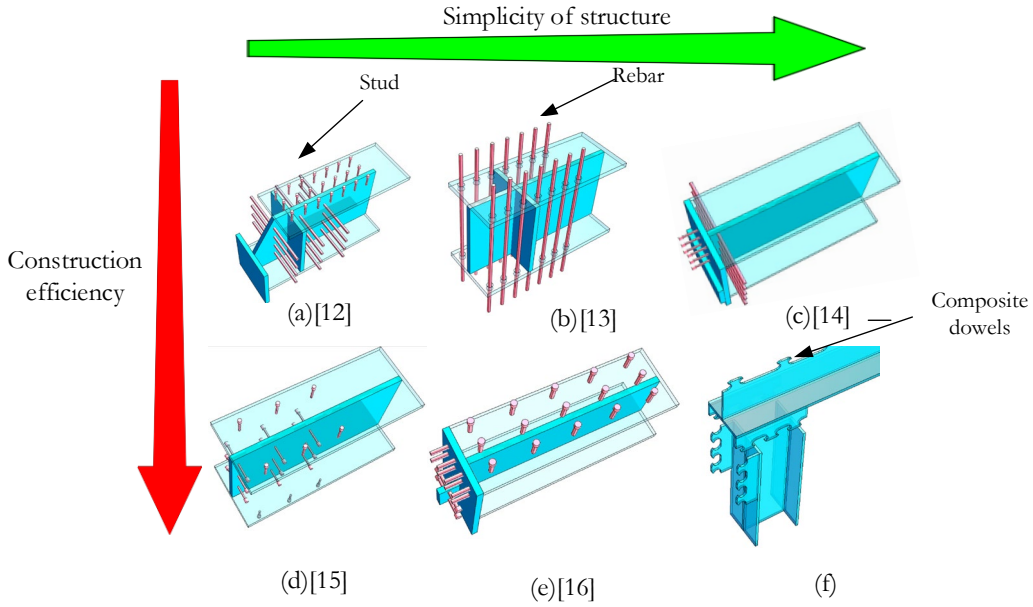

Figure 1: Structural details of the joints.

In previous studies on typical steel girder-concrete abutment joints, two critical factors need attentions: the load-bearing capacity of the abutment joint and its ability to accommodate long-term thermal deformations. The joint must support vertical deck loads while maintaining sufficient flexibility to adapt to temperature-induced displacements [17-18]. Steel-concrete composite girders, when subjected to solar radiation and thermal cycling, experience uneven heat transfer, rendering the deck highly sensitive to temperature variations. Under extreme conditions, thermal effects may dominate over dead and live loads. Research indicates that temperature-induced elongation in jointless bridges can be predicted based on total temperature change [19], with bridge expansion length proportional to its total length, temperature variation, and coefficient of thermal expansion, typically distributed symmetrically at both ends [20].

However, in terms of steel-concrete composite dowel girder-abutment in this work, current integral bridge design codes don't cover. Furthermore, comprehensive concerns on the ultimate bending resistance, failure mechanisms, and load transfer modes of such systems—particularly those incorporating H-shaped steel pile flexible foundations under thermal effects remain addressing. Under this background, we propose an innovative integral abutment integrating composite dowels girder and connectors into the steel girder web, combined with H-shaped steel piles. This configuration enhances the interfacial bond between the concrete deck slab and steel girder while facilitating reinforcement bar penetration, thereby improving both construction efficiency and mechanical performance.

INTEGRAL BRIDGE ABUTMENT WITH COMPOSITE DOWELS

The novel integral abutment is consisted of Modified-Verbund-Fertigteil-Trager (MVFT) girder[10] and composite dowels connections, which is illustrated in Fig.1(f) and Fig.2. The open geometry of CLothoid (CL)-shaped connectors allows reinforcements to be directly threaded through predefined positions during construction, effectively resolving challenges such as rebar penetration difficulties and concrete casting dead zones. Composite dowels are classified as ductile shear connectors [21], particularly suitable for steel-concrete composite sections without flanges. To enhance the bond between the steel pile and abutment, composite dowels are set in the tension zone of the H-shaped steel piles.

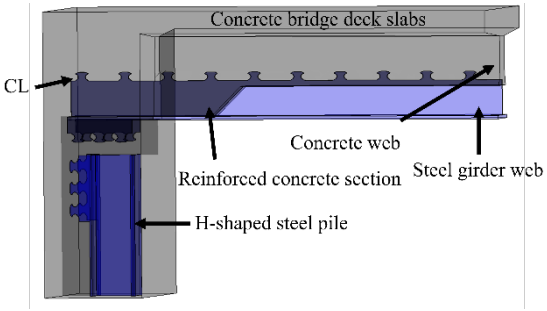

Figure 2: General configuration of the integral abutment.

NUMERICAL STUDY

The Finite Element (FE) model consists of five primary components: the concrete abutment, composite dowel girder, composite dowels, steel reinforcement, and H-shaped steel piles. The FE model, scaled at a ratio of 1:3, is shown in Fig. 2. The concrete abutment measures 800 mm in length and 500 mm in width along the bridge's longitudinal direction.

To account for contact interactions as well as material and geometric nonlinearities, the dynamic explicit method is adopted for the analysis. The quasi-static loading of the concrete abutment and steel girder is simulated using C3D8R elements, while the reinforcement is modeled with T3D2 elements. Given the complexity of the steel-concrete girder structure, localized mesh refinement is applied around the composite dowels to enhance accuracy, with a minimum element size of 10 mm.

For interaction definitions, the rebar is embedded within the abutment using the Embedded Region constraint. Since the composite dowels and the steel girder web can be fabricated from a single steel plate, they are modeled as a single integrated part. The interface between the steel reinforcement and surrounding concrete is also defined using the Embedded Region

approach. The contact between the steel girder and concrete is modeled as hard contact in the normal direction, while tangential behavior is simulated using a penalty-based friction model. The 3D model of steel girder and abutment is demonstrated in Fig. 3.

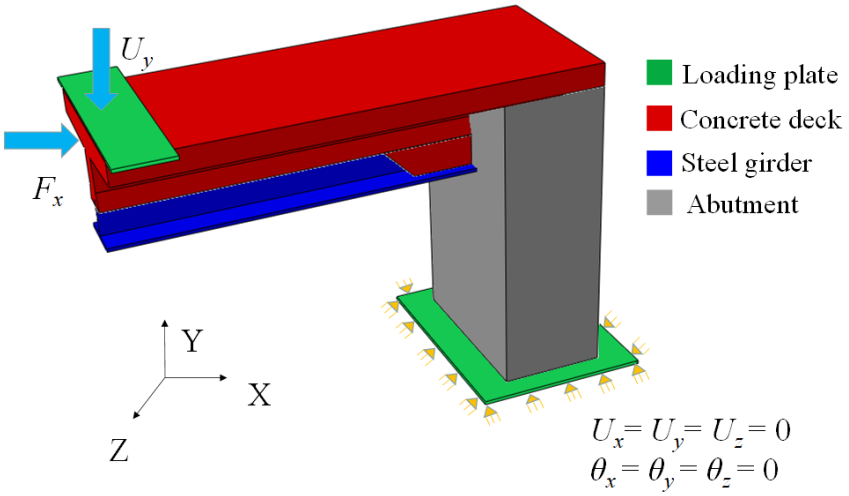

Figure 3: Numeric model of integral abutment.

VERIFICATION MODEL

To validate the accuracy of the FE model, a third-party experimental test was selected. Fig. 4 presents the elevation and side-view dimensions of the joint in the referenced test [21]. The front of the abutment includes a 30 mm thick pressure plate. The steel girder has a depth of 540 mm, with the upper and lower flanges and web each measuring 20 mm in thickness. The main girder is embedded 500 mm into the abutment. Near the front of the abutment, 50 mm diameter holes are provided in the flanges and web, spaced at 120 mm intervals. PBL connectors, consisting of 20 mm diameter steel bars, are inserted into these holes.

The verification model is developed based on the experimental setup, as shown in Fig. 4. Results indicate that the load-displacement response of the FE model closely matches the experimental data when the friction coefficient is set to 0.3. In the model, all degrees of freedom at the constrained rigid reference point are restricted, except for rotation about the Z-axis. Displacement control is employed to prevent sudden failure, which could lead to excessive element deformation and affect ultimate load results.

To ensure consistency with the shear span ratio of the integral bridge and previous studies [22], a loading plate (modeled as an analytical rigid body) is positioned 1.75 times the deck depth from the abutment's front end and is rigidly connected to the deck. A displacement load is applied to the rigid body, with a prescribed forced displacement of 100 mm at the reference point of the loading plate to impose loading on the model. The ultimate load is defined as the maximum vertical reaction force of the loading plate during loading. A smooth amplitude curve is used for loading, and the dynamic internal energy ratio is controlled within 5% to ensure numerical stability.

For material modeling, the Concrete Damaged Plasticity model is used for concrete, with its constitutive behavior based on the General Design Code for Concrete Structures. Steel components are modeled using a bilinear strain-hardening constitutive model, following Eurocode 3 (2006). The material parameters are detailed in Tabs. 1 and 2.

Materials	E/GPa	ν/MPa	σ_s/MPa	f_t/MPa	f_c /MPa
C50	27.100	0.2	—	—	50
Q345	206.000	0.3	345	500	—
Q460	206.000	0.3	460	600	—
HRB400	206.000	0.3	400	500	—

Table 1: Elastic properties

Materials	α/(°)	Strain deviator	f_{b0}/f_{c0}	K	Coefficient of viscosity
Concrete	25	0.1	1.16	0.6667	0.0005

Table 2: Plastic properties.

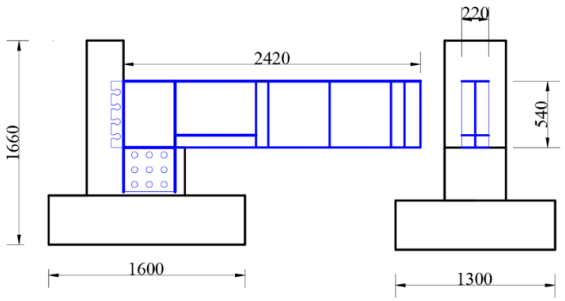

Figure 4: Dimensions of girder-abutment test [21] (Unit: mm).

Concrete	Elasticity modulus	31600
	28-day cylinder f_c	43.2
	28-day cube f_c	52.9
Q345	Elasticity modulus	198000
	Yield strength	391
	Ultimate strength	545
HRB400	Elasticity modulus	202000
	Yield strength	390
	Ultimate strength	485

Table 3: Material parameters (MPa).

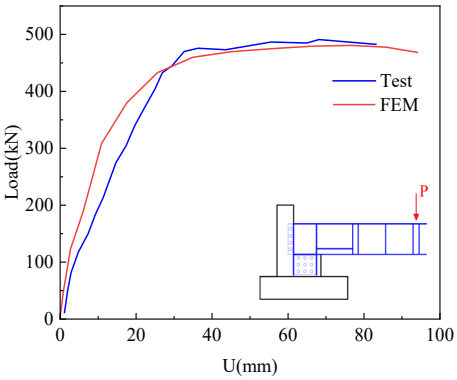

Figure 5: Validation of FE results.

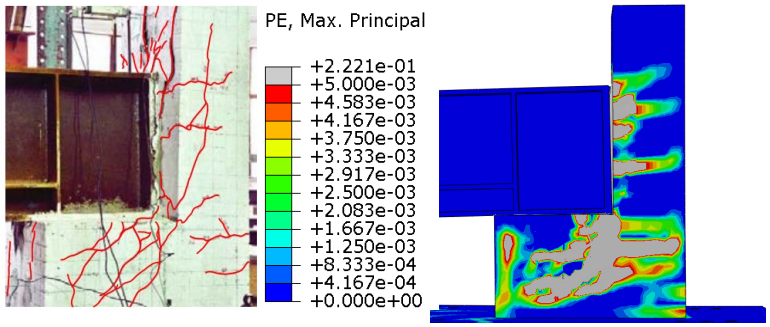

Figure 6: Comparison of failure modes in test and FE results.

As shown in Figs 5 and 6, the FE results closely match the experimental data from the third-party test. The numerical model exhibits slightly higher stiffness after entering the elastoplastic stage, which may be attributed to the absence of early-stage steel-concrete bonding in the ABAQUS model. In the model, the frictional force compensates for this bonding effect. In the experiment, the adhesive force disappears once the component enters the elastoplastic stage, while friction continues to influence the ABAQUS model, resulting in higher stiffness in the early and mid-stages of the FE analysis. Overall, the modeling approach is consistent with the experimental observations.

Fig. 8 illustrates the failure of the concrete in the numerical results, represented by the maximum plastic principal strain contour, which also aligns well with the experimental findings. The numerical model shows the steel girder's pull-out behavior, with cracks forming at the front of the platform and shear cracks along the side of the abutment, accurately simulating the observed failure modes.

TEMPERATURE EFFECT

The minimum and maximum temperatures are key factors influencing the temperature effects on the structure. For the structure shown in Fig. 2, the temperature effect is specifically considered. Summer, being the hottest season of the year, exhibits the most significant temperature impact on bridges. To assess this, the monthly maximum and minimum temperature data for Xi'an over the past five years are analyzed, as shown in Fig. 7.

Correlation analysis and calculations were performed using MATLAB, with the Gevfit function applied to model the generalized extreme value (GEV) distribution. This approach analyzes the extreme temperature values to predict representative load values. The analysis assumes that the temperature samples are independent random variables, each following the same distribution. The generalized extreme value distribution is expressed by Eq. (1), where the representative values of the highest and lowest temperatures are 37.5°C and 15.7°C, respectively.

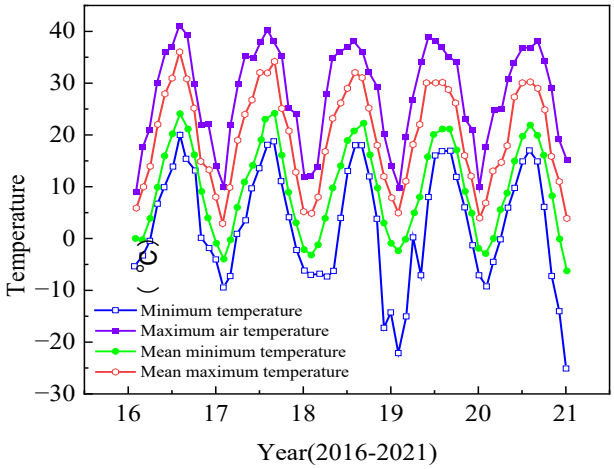

Figure 7: Monthly temperature data of Xi 'an in recent 5 years.

$$H=\exp\left\{-\left(1+\zeta\frac{x-\mu}{\sigma}\right)^{-1/\zeta}\right\},\ 1+\zeta\frac{x-\mu}{\sigma}>0 \tag{1}$$

where x is the random variable, μ is the position parameter, σ is the scale parameter, ζ is the shape parameter, and the last three parameters are determined by the selected sample.

The maximum horizontal force of the temperature effect of the integral jointless bridge on the abutment and the following parameters are required according to [22]:

Abutment height H=2.6m, deck width B=1.6m, span length L=20m, unit weight γ=18kN/m^3, T_{max}=37.5℃, T_{min}=15.7℃, Coefficient of thermal expansion of concrete α=10×10^{-6}/℃. If calculated as beginning from zero, the horizontal spring for the whole abutment would be:

$$k=\frac{p}{\Delta L}=\frac{H}{2}\cdot\gamma\cdot 1.3\cdot H\cdot B/0.003=16224kN\cdot m \tag{2}$$

$$\Delta L\cdot k+F=372.7\ \text{kN} \tag{3}$$

PARAMETRIC ANALYSIS

A parametric analysis was conducted to examine the influence of various abutment parameters, including steel type, plate thickness, bridge deck reinforcement ratio and composite dowel spacing. Based on the General Design Code for Concrete Structures (GB 55008-2021), the parameters were set as follows:

Steel type: Q345, Q460; Steel plate thickness (t): 16–24 mm; Composite dowel spacing (e_x): 200–800 mm;

Bridge deck reinforcement ratio (ρ_1): 1.01%, 1.52%, 2.11%; Deck width (w_s): 400–600 mm; Abutment longitudinal width (wc): 750–1500 mm; Abutment reinforcement ratio (ρ_2): 0.8%–1.2%.

To validate the parametric study, a pilot integral abutment with composite dowels was designed and analyzed. The span of the integral abutment bridge with composite dowel girders is L = 20 m. The deck consists of four girders, each B = 1.6 m wide, as illustrated in Fig. 8. The total deck width is 8.5 m, while the concrete abutment has a longitudinal width of 0.9 m and a height of 2.6 m. The H-shaped steel piles are of type HW400×400×20×20 mm.

A three-dimensional finite element model of the integral abutment joint, composite girder, and H-shaped steel piles was developed using ABAQUS. The load-bearing performance and failure mechanisms of the integrated joint were then systematically investigated. Here, H represents the composite girder height, while h denotes the steel girder height.

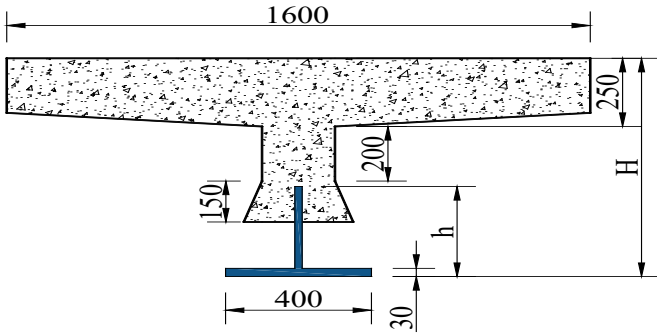

Figure 8: Cross-section of composite dowels girder (mm).

INFLUENCE OF PARAMETERS OF COMPOSITE DOWELS GIRDER

As shown in Fig. 9, increasing the steel strength of the composite dowel girder from Q345 to Q460, while keeping other parameters constant, results in a slight improvement in ultimate bearing capacity. For a girder height of 800 mm, the ultimate bearing capacity increases from 559 kN to 592 kN, representing a 5.9% increase. For a 1000 mm girder, the capacity rises from 652 kN to 675 kN, an increase of 3.5%. These results indicate that the ultimate bearing capacity of high-depth steel-concrete composite girders with composite dowels is minimally affected by steel strength. Therefore, a more economical steel grade can be selected without significantly compromising the load-bearing performance. As illustrated in Fig. 10, the bearing capacity of the steel girder base plate increases by 2.4% when its width expands from 400 mm to 500 mm, and by 12% when further increased to 600 mm. According to design specifications, the base plate width can be set at either 400 mm or 600 mm, depending on load-bearing requirements. A 400 mm width is suitable for lower design standards, whereas a 600 mm width is preferable for higher load-bearing demands.

As depicted in Fig. 11, for girder depths of 800 mm and 1000 mm, the ultimate bearing capacity does not increase with changes in web thickness or composite dowel spacing. The failure mode analysis reveals that the structure ultimately loses its load-bearing capacity due to concrete crushing beneath the floor, rather than limitations in the steel girder web.

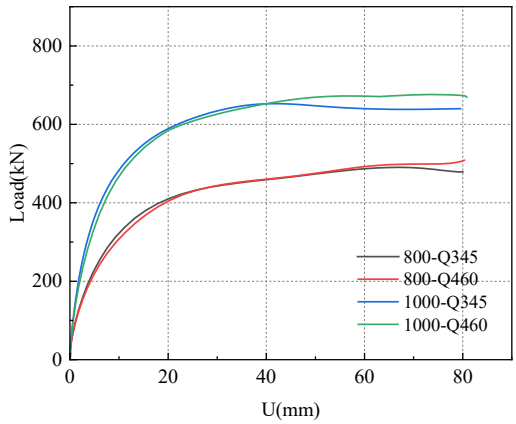

Figure 9: Effect of the steel strength of composite dowels girder.

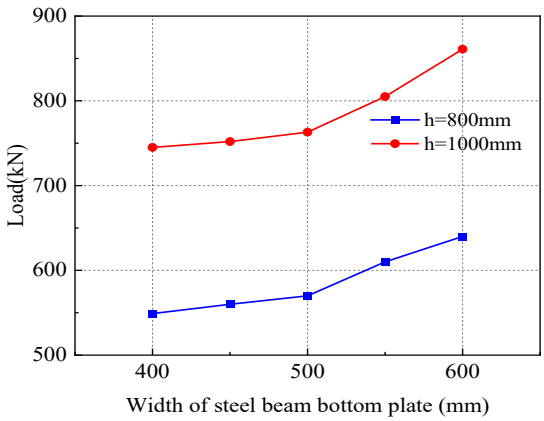

Figure 10: Effect of the width of steel girder bottom plate.

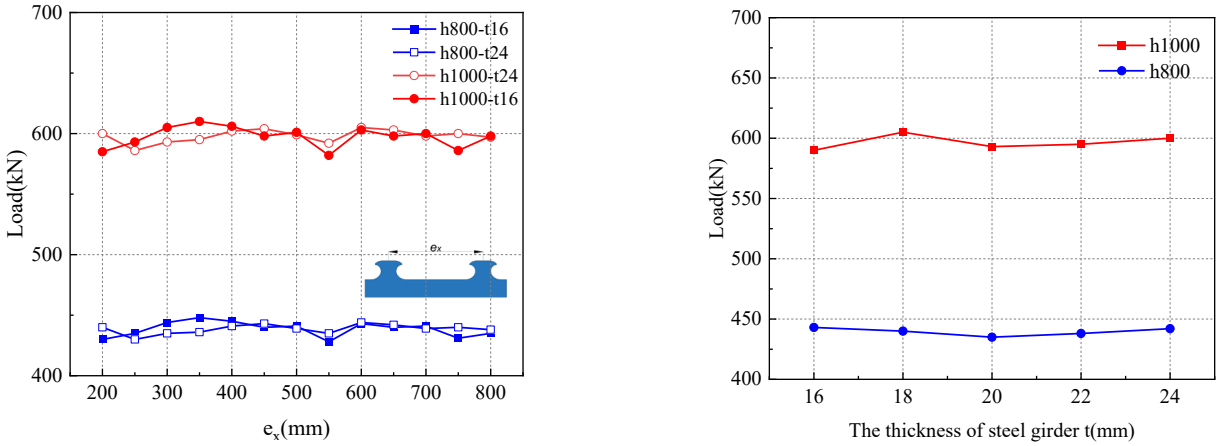

Figure 11: Effect of the center distance of composite dowels(a) and thickness of steel girder (b).

Three composite dowel arrangements were evaluated for embedding into the steel girder bottom plate at the bridge end:
CL-1: Dowel spacing e_x=200 mm, with two rows spaced 260 mm apart at the girder end.
CL-2: Dowel spacing e_x=200 mm, with a horizontal arrangement of three rows, spaced 100 mm apart at the girder end.
CL-3: No composite dowels arranged.
Tab. 4 compares the bearing capacities of these configurations, showing that CL-2 outperforms the other arrangements. Compared to CL-1, CL-2 improves bearing capacity by 2.3%, while compared to CL-3, it increases by 6.1%. Despite featuring three rows of dowels, CL-2 does not compromise construction feasibility, making it the recommended configuration.

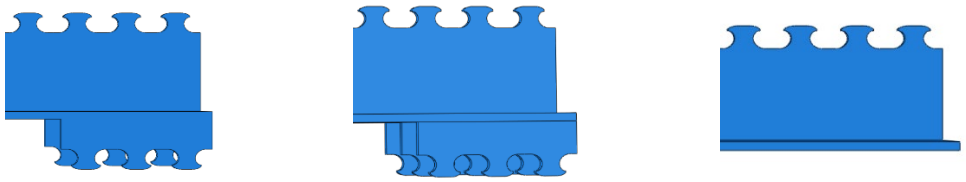

	CL-1	CL-2	CL-3
RF	655	670	632

Table 4: Composite dowels combinations.

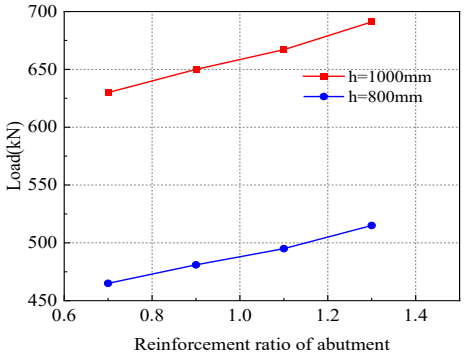

Figure 12: Effect of reinforcement ratio of abutment

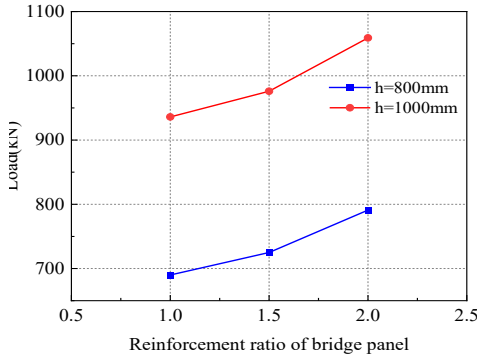

Figure 13: Effect of reinforcement ratio of deck ϱ_2

INFLUENCE OF REINFORCEMENT RATIO

Fig. 12 shows the effect of the reinforcement ratio of the abutment (ϱ_1) on the joint's load-bearing capacity. The results indicate a significant correlation between ϱ_1 and the structural performance of the joint. Specifically, when ϱ_1 increases from 0.7% to 1.5%, the ultimate bearing capacity of the joint improves by approximately 11%.

Similarly, Fig. 13 presents the influence of the reinforcement ratio of the deck (ϱ_2) on the joint's load-bearing capacity. The analysis reveals that when ϱ_2 increases from 1% to 2%, the joint's bearing capacity enhances by approximately 13%. These findings highlight the crucial role of reinforcement in improving the structural integrity and performance of the integral abutment joint.

INFLUENCE OF LONGITUDINAL BRIDGE WIDTH ON ABUTMENT W_C

As is shown in Fig.14, the longitudinal bridge width (750–1500 mm) exhibits a linear relationship with the overall bearing capacity of the joint. When the width increases from 750 mm to 1500 mm (a 100% increase), the bearing capacity improves by 35.8%. These findings suggest that the longitudinal bridge width of abutments can be optimized based on the specific requirements of the project to achieve the desired structural performance.

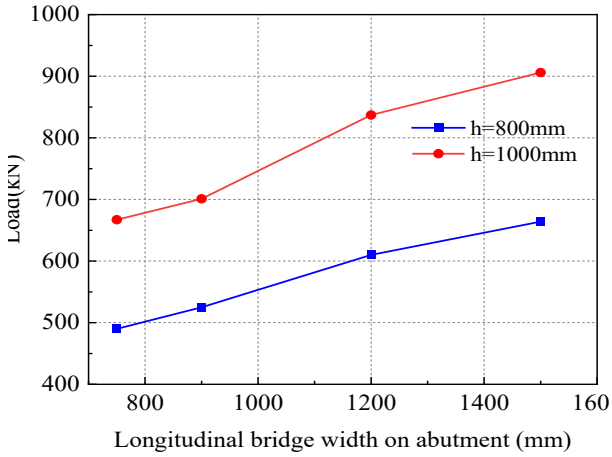

Figure 14: Effect of longitudinal bridge width on abutment.

FAILURE PATTERNS AND LOAD-TRANSITION MECHANISM - FAILURE PATTERNS

The failure modes of the joint are illustrated in Fig.s 15–18. In the finite element results, concrete failure is represented by the maximum plastic principal strain contour, where white areas indicate severe cracking. The steel girder failure is depicted using the longitudinal strain contour of the bridge.

As shown in Fig. 15, the stress distribution and 3× deformation amplification of the steel girder at failure reveal that the web experiences significant strain, while the bottom plate and ends of the web undergo compression. Due to high stress, the bottom plate near the front of the abutment deforms significantly. During loading, the neutral axis of the steel girder section gradually moves downward, leading to rotation around the bottom plate near the front of the abutment. This results in cracks forming in the concrete web. The web plate of the embedded steel girder section is primarily subjected to shear forces, exhibiting significant shear stress. The relative angle between the inserted section and the extended section of the steel girder indicates strong interaction with the concrete abutment, demonstrating the high connection performance and tensile resistance of the composite dowels. Throughout the loading process, the integral abutment joints are subjected to large bending moments and shear forces, ultimately causing cracks in the concrete web due to excessive tensile and compressive stresses at the steel-concrete interface. As the external load increases, the number and width of cracks progressively expand.

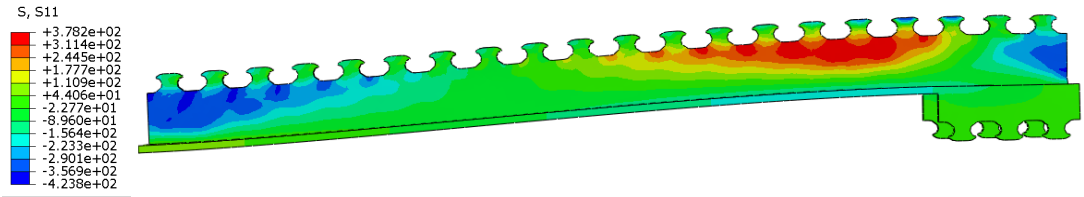

Figure 15: Stress and deformation of steel main girder (MPa).

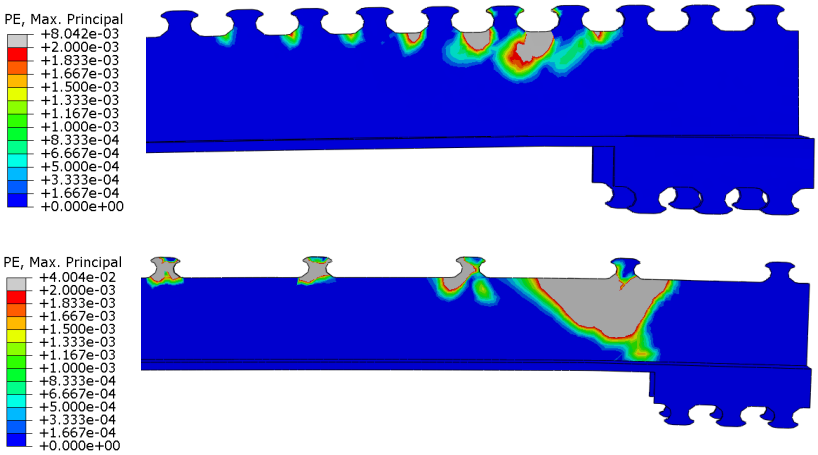

Figure 16: Plastic strain contour of steel girder.

Fig. 16 presents the plastic strain contours of steel girders for ex = 200 mm and ex = 600 mm when the joint reaches its ultimate bearing capacity, highlighting the failure modes. As ex increases, the plastic region at the interface between the embedded steel girder section and the extended section expands from the web to the bottom plate, creating a weakened section. Additionally, the tooth joints yield, and local crushing of concrete under the steel girder occurs once the weakened section reaches full plasticity.

According to the failure patterns of the concrete component shown in Fig. 17, tensile cracks initially develop at the top of the rear abutment due to its high stiffness and the rotation of the extended steel girder section. As loading continues, these cracks propagate, particularly in the concrete surrounding the composite dowels, caused by the rotation of the steel girder and concrete compression between the dowels. These cracks gradually extend toward the deck. With further loading, tensile stresses induce cracking in the deck, which spreads at an inclined angle toward the junction of the main girder and steel piles. The cracks on the abutment are shown in Fig. 18.

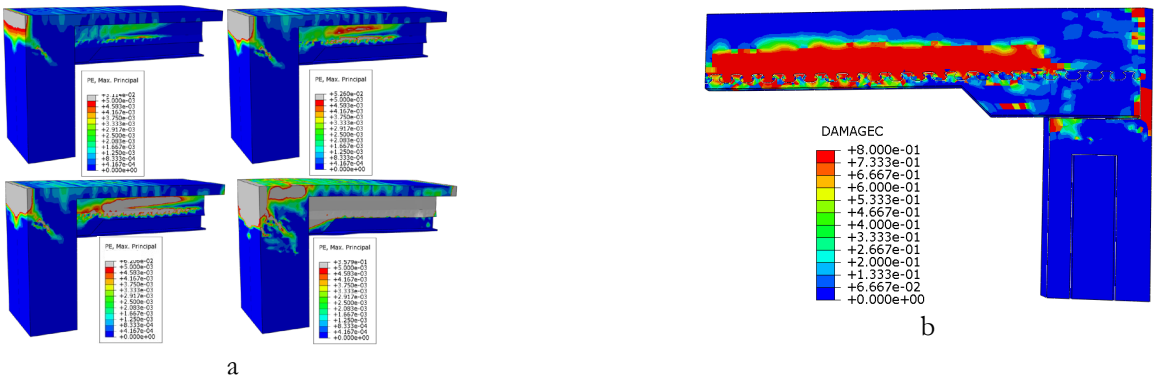

Figure 17: Failure mode.

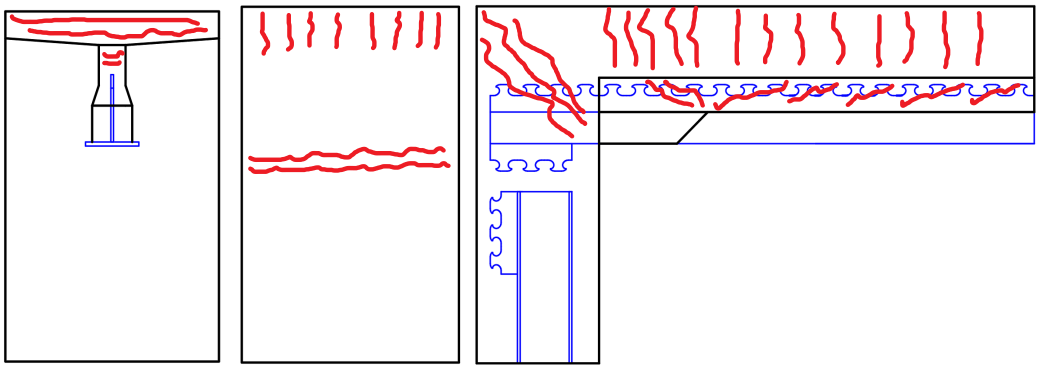

Figure 18: Crack distribution.

During loading, the bending moment and shear force in the steel girder exceed its capacity, causing plastic deformation and yielding near the front of the abutment (Fig. 16). Eventually, concrete crushing beneath the steel girder base plate leads to structural failure. This phenomenon highlights the importance of considering steel-concrete interaction and their load-bearing properties under various stress states when designing composite girder structures.

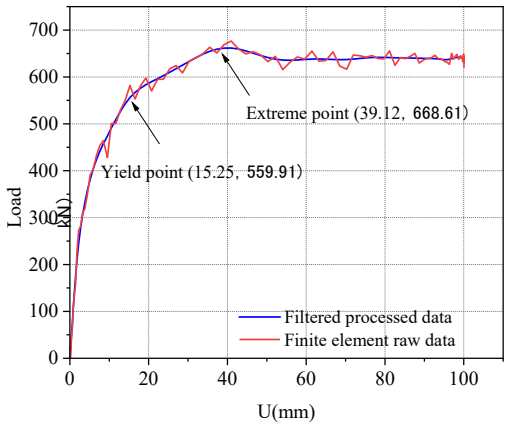

Figure 19: Load-displacement curve.

To mitigate dynamic noise interference, the load-displacement curve was filtered (Fig. 19). After processing, the yield and ultimate points are more distinctly visible and align well with the original data. The yield point is determined as the tangent intersection between the line connecting the extreme point to the origin and the load-displacement curve.

In general, at the initial stage of loading, the abutment exhibits insignificant deformation, remaining within the elastic stage until reaching the yield point. As displacement increases, the bearing capacity gradually declines post-peak, forming a plateau region. This behavior occurs due to collapse of the concrete between composite dowels, surrounding concrete cracking, and shear resistance loss, while the penetrating steel bars between composite dowels continue to resist shear forces.

After reaching the peak load, the bearing capacity does not sharply decline, but deformation accelerates, demonstrating good ductility characteristics. The main girder concrete, abutment cracks, steel girder deflection, and reinforcement deformation progressively increase. Ultimately, the structure loses its load-bearing capacity due to: 1) Concrete crushing beneath the steel girder base plate; 2) Concrete web cracking; 3) Steel girder buckling.

LOAD-TRANSFERRING MECHANISM

As shown in Fig. 20, the stress on the composite dowels within the steel girder is minimal and does not reach the yield state. The stress beneath the composite dowels on the steel web is generally lower than that between the composite dowels. The composite dowels on the web do not directly contribute to the bearing capacity but enhance the collaborative load-bearing effect between the steel girder and the concrete. However, as the spacing between the dowels decreases, the stress on the composite dowels increases, although it remains significantly smaller than the stress on the steel girder web.

Fig. 20 and Fig. 21 demonstrate that the top section of the concrete abutment is damaged due to the action of the negative bending moment at the joint, where the steel girder acts as a lever. The concrete in the damaged area experiences a combination of tensile yield in the upper part and compression in the lower part. The external load is primarily resisted by three components of the joint: the concrete between the composite dowels, the steel bars in the concrete deck slab, and the concrete at the contact surface of the main girder. In the elastic stage, the bending moment from the external load is primarily borne by the steel girder's bottom plate. As the load increases, the steel web and joint enter the elastoplastic stage, the relative angle increases rapidly, and the load is gradually transferred to the steel bars in the deck.

When the plastic region of the steel girder web reaches its maximum, the joint enters the failure stage. The contact force between the steel girder bottom plate and the concrete decreases, and the load is predominantly borne by the concrete beneath the steel girder. With further load increase, the concrete beneath the steel girder is crushed, leading to the failure of the joint.

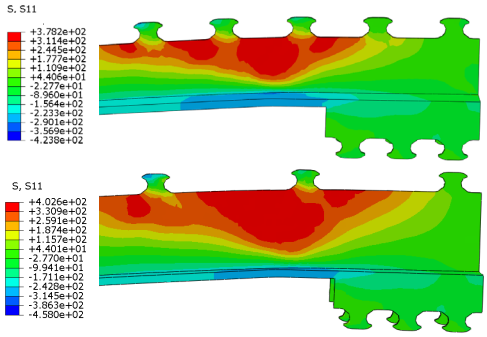

Figure 20: Local stress of composite dowels at failure

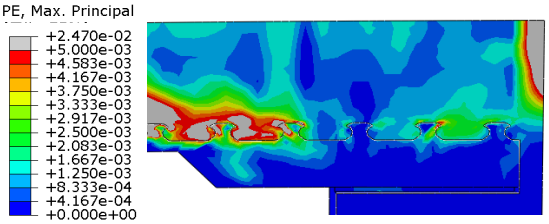

Figure 21: Local strain of concrete at failure

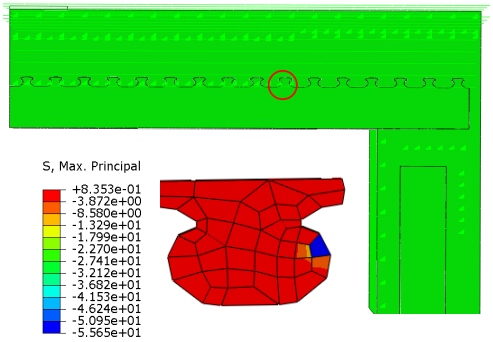

Figure 22: Stress of concrete and rebars between composite dowels.

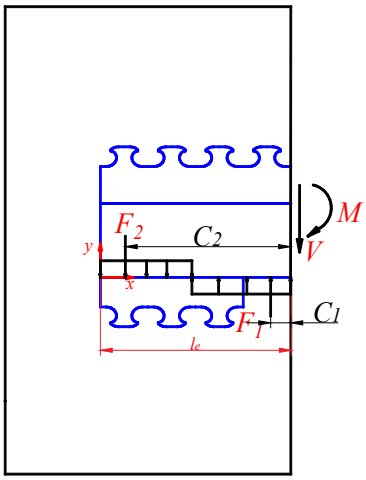

Figure 23: Force transmission of nodes

Fig. 22 shows the maximum principal stress distribution in the concrete between the composite dowels under the ultimate load. It can be observed that the concrete in the hole experiences hydro-compression due to the constraints imposed by the surrounding concrete blocks and the presence of penetrating rebars. Therefore, during operation, the rebars within the composite dowels primarily experience shear stress, while the concrete between the dowels is subject to compressive stress. Based on Fig. 17 and Fig. 23, the primary stress transfer occurs at the contact point between the steel girder and the concrete beneath the plate. The shear force at the front surface of the platform, denoted as V, represents the joint's shear capacity. The forces F_1 and F_2 are the equivalent concentrated forces acting in the compression area of the steel girder, while M denotes the bending moment of the steel girder at the front surface of the platform, indicating the joint's bending capacity. C_1 and C_2 represent the positions of the equivalent concentrated forces in the compression area of the steel girder.

THEORETICAL ANALYSES OF THE FLEXURAL BEARING CAPACITY OF JOINTS – ASSUMPTIONS

Based on the theoretical analysis of the flexural bearing capacity of the joint of steel girder and concrete abutment, the following assumptions are adopted herein:

1) Regardless of the adhesion and friction between the steel girder and the concrete abutment; 2) The assumption that the buried steel girder is regarded as a rigid body which is often used in the analysis of joints without connectors. When the connectors are set, the assumption is more realistic because the buried steel girder is shorter and has higher stiffness. Under the above assumptions, the compressive stress at the top and bottom of the steel girder is linearly distributed, and the peak strain ε_{cl} and ultimate strain ε_{cu} are 0.002 and 0.003, respectively.

$$\varepsilon_b=0.03(le\text{-}c)/c \tag{4}$$

The force diagram of the joint in the limit state is demonstrated in Fig.24. The failure mode of the joint is assumed to be crushed concrete under the steel girder, and the other failure modes are not discussed this time. This requires $\varepsilon_b < 0.003$ in the limiting state. Under this condition, ε_b of alternative Eq. (4) can obtain $c/l_e > 0.5$.

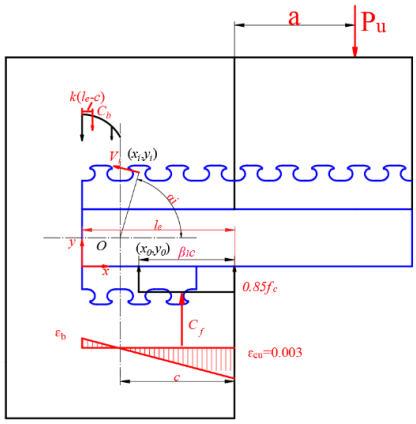

Figure 24: Force transferring diagram in the limit state.

The stress-strain relationship of concrete is assumed to be:

$$\sigma_c = \begin{cases} 1000 f_c(\varepsilon - 250\varepsilon^2), 0 < \varepsilon \leqslant \varepsilon_1 \\ f_c \qquad\qquad\qquad\quad , \varepsilon_1 < \varepsilon \leqslant \varepsilon_{cu} \end{cases}^s \tag{5}$$

The bending capacity of the steel girder-concrete joint is assumed to be the sum of the bending moment contribution of the bearing action and the bending moment contribution of the connector, namely:

$$M_u = P_u(a+c) = M_c + M_s \tag{6}$$

DETERMINATION OF THE ROTATION CENTER

As shown in Fig. 24, the horizontal and vertical point lines are the parts where the vertical and horizontal relative displacements of steel girder and concrete abutment are zero respectively, and the center of deformation and rotation O is defined as the intersection point of these two lines. The balance equation combining vertical direction and horizontal direction in the ministry is as follows:

$$C_b + \sum_{i=1}^{n} v_i^y - C_f + P_u = 0 \tag{7}$$

Make $\lambda = c/l_e$, $\mu = a/l_e$
Previous studies have concluded that:

$$M_C = C_b(1-k)(l_e - c) + C_f\left(c - \frac{1}{2}\beta_1 c\right) \tag{8}$$

When $\lambda \geq 0.6$,

$$C_b = \frac{3}{4} f_c b l_e \left(\frac{1-\lambda}{\lambda}\right)^2 (3\lambda - 1) \tag{9}$$

$$C_f = 0.85\beta_1 f_c b l_e \lambda \tag{10}$$

$$k = \frac{2.75\lambda - 0.75}{9\lambda - 3} \tag{11}$$

When $0.5 < \lambda \leq 0.6$,

$$C_b = f_c b l_e \left(1 - \frac{11}{9}\lambda\right) \tag{12}$$

$$C_f = 0.85\beta_1 f_c b l_e \lambda \tag{13}$$

$$k = \frac{13.5 - 33\lambda + 20.5\lambda^2}{27 - 60\lambda + 33\lambda^2} \tag{14}$$

Subdivision point λ=0.6, corresponding to Eq. (3) in $\varepsilon = \varepsilon_n l$.
It can be seen that λ is related to the bending moment contribution of the CL and the arrangement form of the CL. The solution for λ is very complex, but it can be inferred that the relative rotation of the center position O at the centroid of the composite dowels and the contribution to the bending moment of the composite dowels can be ignored without timing being obtained:
When λ≥0.6,

$$\begin{aligned}(55 - 34\beta_1^2)\lambda^4 + (180 - 68\beta_1)\mu\lambda^3 + (-420\mu - 210)\lambda^2 + \\ (330\mu + 200)\lambda - (60\mu + 45) = 0\end{aligned} \tag{15}$$

When $0.5 < \lambda \leq 0.6$,

$$\left(\frac{17}{40}\beta_1^2 + \frac{41}{54}\right)\lambda^2 + \left(\frac{11}{9} + \frac{17}{20}\beta_1\right)\mu\lambda - \mu - 0.5 = 0 \tag{16}$$

Mattock [23] assumed that μ is between 0.1-0.5, and calculated the relationship through Eq. (13). λ deviated little from its mean value of 0.66, so λ was taken as 0.66 in the design. Liang found that for the joints of integral bridges, however, μ between 0.1-0.5 is lower and should be between 1-10, and the value of β ranges from 0.65-085. Corresponding to the compressive strength of concrete axis 28-56MPa [21]. The mean is 0.56 as the value of λ, and the standard deviation is 4.4% Therefore, the coordinates relative to the center of rotation O are:

$$x_0 = 0.44 l_e \tag{17}$$

$$y_0 = \frac{1}{n}\sum_{i=1}^{n} y_i \tag{18}$$

CONTRIBUTION FROM GIRDER

Since λ=0.56 and $0.5 < \lambda \leq 0.6$, C_b, C_f and k in Eq.(6) are replaced by Eqn. (10)-(12)

$$M_c = 0.85 f_c b l_e^2 (0.314\beta_1 - 0.157\beta_1^2 + 0.100) \tag{19}$$

The maximum local stress f_b of concrete under the limit state is assumed to be 0.85 f_c in the above calculation, but the actual f_b is related to the ratio of the width of the concrete abutment to the width of the steel girder (w/b). f_b can be expressed as:

$$f_b = K(f_c)^a \left(\frac{w}{b}\right)^c \tag{20}$$

	Mattock[23]	Tschemmernegg[24]	Eurocode 2: -part 1–1	Hawkins[25]
K	4.5	4.5	< 1.0	4.5
a	0.5	0.5	1.0	0.5
c	0.66	0.55/0.60	0.50	0.33
Range	$w/b \leq 12$	$w/b \leq 4.5$	$f_b \leq 3.0 f_c$	-

Table 5: Summarizes the coefficient values of f_b calculated in the literature

In this paper, $w/b=4$ is selected based on the biased safety angle:

$$f_b = 4.5\sqrt{f_c}(w/b)^{0.66} \tag{21}$$

replacing 0.85 f_c in Eq. (17) with Eq. (19), when β_1 varies between 0.65-0.85,$2\beta_1-\beta_1^2+0.637$is the mean value of 1.5645, and the maximum error is 3.3%.

$$M_C = 1.106 l_e^2 \sqrt{f_c b w} \tag{22}$$

CONTRIBUTION FROM COMPOSITE DOWELS

The bearing capacity of a single composite dowel is determined according to [11], namely:

$$F_e = 2.6 \cdot \eta_s \cdot k \cdot \sqrt{f_{cm} c_{D,S}} \cdot \sqrt[3]{t h_{d,eff}} \cdot \sqrt[3]{e_x} \tag{23}$$

The symbols are described as:

η_s reinforcement stirrup coefficient, 1 stirrups: η_s=0.9,2 stirrups: η_s=1 ,3stirrups: η_s=1.1;
k size effect factor: k=1+(200/ $c_{D,S}$)$^{0.5}$;
f_{cm} compressive strength of the concrete (MPa);
$c_{D,S}$ compressive strength of the concrete (m);
t steel thickness (m);
e_x center distance of the composite dowels (m);
$h_{d,eff}$ effective steel tooth height (m).

The bearing capacity of all composite dowels joints in the joint is assumed to be a polynomial relationship between F_S and F_e:

$$F_S = F_{N,FEM} - F_C \tag{24}$$

CONTRIBUTION FROM REINFORCEMENT RATIO

In Fig. 25, the red part is the parameter sensitive region, and the blue part is the insensitive region. As mentioned above, the abutment reinforcement ratio ρ_1 increases from 0.7% to 1.3%, and the bearing capacity increases by about 3% with a change of 0.2 percentage points. The influence coefficient Z_a of the abutment reinforcement ratio can be defined

as:1-1.11(0.7% to 1.3%). The abutment reinforcement ratio ϱ_2 increases linearly by 14% from 1% to 2%, and an impact factor Z_p 1-1.13 (1% to 2%) can be defined.

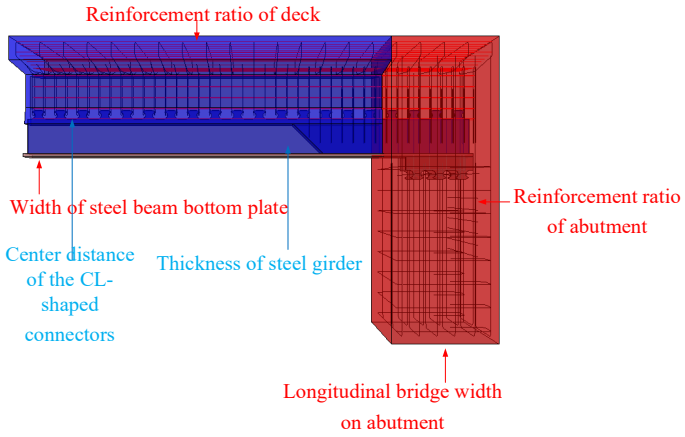

Figure 25: Reinforcement Sensitivity Distribution.

BEARING CAPACITY FORMULA

Through the fitting of 180 sets of numeric results plus theoretic analysis, the ultimate bearing capacity formula of the integral abutment joint is constructed as follows.

Given the concrete slab reinforcement ratio, the capacity formula is defined as:

$$F_N = Z_a Z_p \cdot F_s \tag{25}$$

The previous section found that the ultimate bearing capacity of 800mm girder is about 74% of that of 1000mm girder. Therefore, a girder depth influence coefficient h, h_{800}=0.74, h_{1000}=1 can be obtained.

$$F_N = Z_a \times Z_p \times \left(421 + 0.43 \times (1.106 l_e^2 \sqrt{f_c bw}/2.9 + F_e) - 0.00014 \times \left(1.106 l_e^2 \sqrt{f_c bw}/2.9\right)^2\right) \tag{26}$$

In Fig.26 F_1 is the finite element result and F_2 is the formula value, it is clear that the ultimate bearing capacity obtained by the formula is very close to the finite element results, and the average error is within 3%.

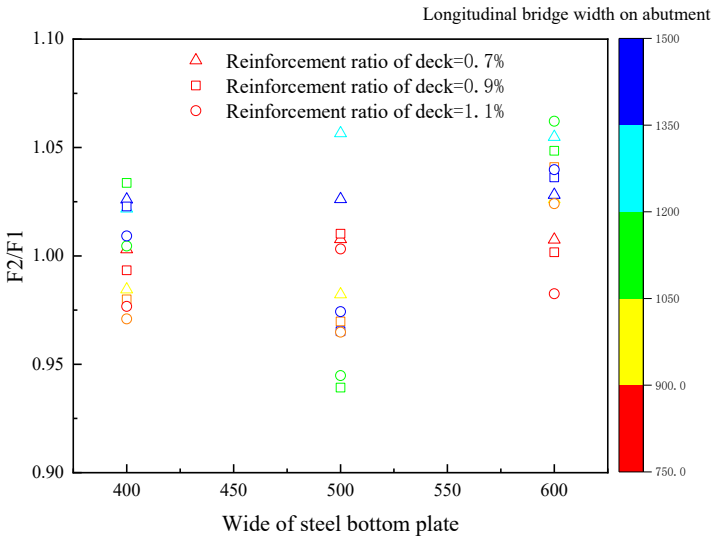

Fig. 26: Comparison between formula results and FE values

Based on the developed formula for the integral abutment, a comparison of bearing capacity and steel consumption between the integral abutment proposed in this work and the traditional I-shaped steel girder with the same size is carried out. In Liang's test [21], the width of the bottom plate of the steel girder is 220 mm, the depth of the steel girder is 540 mm, the embedding depth of the steel girder is 360 mm, the reinforcement rate of the abutment is 0.72%, the width of the abutment is 500 mm, and the ultimate bearing capacity of the test is 488 kN. The size of the steel girder in this paper was adjusted to match that in the test. Employing the calculation formula proposed in this paper, the ultimate bearing capacity is calculated as 507 kN. It is found that the bearing capacity at the girder-joint mainly relies on the longitudinal tensile bearing capacity provided by the bridge deck reinforcement, while the concrete at the contact surface between the steel girder and the concrete abutment transfers the external load through compression. Compared with the traditional I-shaped steel girder in the experiment, under the same steel girder depth and bottom plate width, the steel consumption of the integral abutment in this paper is reduced by 23%. This saving arises in part because the longitudinal reinforcement was not included in Liang's test [21]. Once the steel girder yielded, it would lose bearing capacity. In contrast, for the integral abutment in this work, the presence of longitudinal reinforcement in the bridge deck and the concrete web allows the steel girder to retain load-bearing capacity even after yielding.

CONCLUSION

- ✓ The failure modes and load transfer mechanisms of the proposed integral bridge abutment with composite dowels are found. Failure initiates with cracking in the concrete surrounding the composite dowels, leading to a loss of shear resistance. However, the penetrating steel bars between the dowels do not yield and continue to carry shear forces. After reaching the peak load, the abutment maintains its bearing capacity without a sharp decrease, though deformation progresses rapidly, exhibiting good ductility. Cracking in the abutment, steel girder deflection, and steel bar deformation increase to varying degrees. Ultimately, failure occurs due to the local yielding of the steel girder.
- ✓ Typical girder dimensions and concrete reinforcement of the integral abutment are suggested. With respect to the girder depth range from 800mm-1000mm, an optimal dowel spacing 300-350mm and web thickness of 20mm are recommended. Additionally, increasing the reinforcement ratio of the abutment from 1% to 2% enhances the joint's bearing capacity by approximately 13%.
- ✓ A formula for the ultimate bearing capacity of the integral abutment joint is proposed, which accounts for contributions from both the composite girder and connections. Validation against numerical results shows an average error below 3%, confirming its accuracy. This formula facilitates rapid design optimization and serves as a reliable tool for engineers to assess the performance of the abutment under multifactorial loading conditions, including thermal effects and seismic actions.

ACKNOWLEDGEMENTS

The authors appreciate the support of Natural Science Foundation of Shaanxi Province (Grant No. 2023-JC-YB-360)

REFERENCES

[1] Pak, D., Bigelow, H., & Feldmann, M. (2017). Design of composite bridges with integral abutments. Steel Construction, 10(1), pp. 23-30.
[2] Mertz, D. (2013). Design Guide for Bridges for Service Life. Strategic Highway.
[3] Paraschos, A. (2016). Effects of wingwall configurations on the behavior of integral abutment bridges (Doctoral dissertation, University of Maryland, College Park).
[4] Pnevmatikos, N. G.,Papagiannopoulos, G. A.,Papavasileiou, G. S. (2019). Fragility curves for mixed concrete/steel frames subjected to seismic excitation, Soil Dynamics and Earthquake Engineering 116, pp. 709-713.
[5] Arsoy, S., Duncan, J. M., & Barker, R. M. (2002). Performance of piles supporting integral bridges. Transportation Research Record, 1808(1), pp. 162-167.

[6] Dreyer, T., Fronek, A., Fataar, H., Mpye, G. D., Skorpen, S., Kearsley, E. and van Zijl, G. (2025). Soil–Structure Interaction Analysis of Transition Zone Deformations due to Imposed Abutment Displacement Cycles in an Integral Bridge. Journal of Bridge Engineering, 30(4), 04025005.
[7] Fiorentino, G., Cengiz, C., De Luca, F., Mylonakis, G., Karamitros, D., Dietz, M. and Nuti, C. (2021). Integral abutment bridges: investigation of seismic soil-structure interaction effects by shaking table testing. Earthquake Engineering & Structural Dynamics, 50(6), pp. 1517-1538.
[8] Kim, S. H., Yoon, J. H., Kim, J. H., Choi, W. J. and Ahn, J. H. (2012). Structural details of steel girder–abutment joints in integral bridges: An experimental study. Journal of Constructional Steel Research, 70, pp. 190-212.
[9] Feldmann, M., Kopp, M. and Pak, D. (2016). Composite dowels as shear connectors for composite girders–background to the German technical approval. Steel Construction, 9(2), pp. 80-88.
[10] Xiong, Z., Pan, Z., Wolters, K., Liu, H., Cheng, L., Li, J. and Feldmann, M. (2024). Prefabricated Composite Dowels Girders for Small Bridges-Structural Design and Efficiency, Evaluation.ce/papers, 7(3-4), pp. 50-62.
[11] Xiong, Z., Li, J., Wolters, K., Mou, X., & Feldmann, M. (2025). Fatigue performance of composite dowels under combination of shear and tension – Part I – Steel component. Steel Construction,18(1), pp. 52-62.
[12] Feldmann, M., Naumes, J., Pak, D., Veljkovic, M., Nilsson, M., Eriksen, J. and Popa, N. (2010). Economic and durable design of composite bridges with integral abutments, European Commission, DOI: 10.2777/91014.
[13] Ashiduka, K., Miyata, H., Sakate, M., Kiso, S., Kurita, A., Shimotaniike, T. and Leistung, P. (2007). Design of hybrid frame bridge having spread foundation and proposal for rationalization of connection detail between steel girder and RC abutment. Kou Kouzou Rombunshuu. A, 53, pp. 936-945.
[14] Riches, O. J., Carstairs, N. A., & Jones, A. E. (2005, June). A simplified integral composite bridge connection. In Proceedings of the Institution of Civil Engineers-Bridge Engineering, 158(2), pp. 63-69).
[15] VTrans Integral Abutment Committee. (2008). Integral Abutment Bridge Design Guidelines, the State of Vermont. Agency of Transportation, Montpelier.
[16] Briseghella, B. and Zordan, T. (2015). An innovative steel-concrete joint for integral abutment bridges. Journal of Traffic and Transportation Engineering (English Edition), 2(4), pp. 209-222.
[17] Far, N. E., Maleki, S. and Barghian, M. (2015). Design of integral abutment bridges for combined thermal and seismic loads. Earthquakes and Structures, 9(2), pp. 415-430.
[18] LaFave, J. M., Riddle, J. K., Jarrett, M. W., Wright, B. A., Svatora, J. S., An, H. and Fahnestock, L. A. (2016). Numerical simulations of steel integral abutment bridges under thermal loading. Journal of Bridge Engineering, 21(10), 04016061.
[19] Kunin, J. and Alampalli, S. (2000). Integral abutment bridges: Current practice in United States and Canada. Journal of performance of constructed facilities, 14(3), pp. 104-111.
[20] Aktan, H., Attanayake, U. and Ulku, E. (2008). Combining link slab, deck sliding over backwall, and revising bearings (No. RC-1514).
[21] Liang, C., Liu, Y., Zhao, C., Lei, B. and Wu, J. (2018). Experimental and numerical study on an innovative girder-abutment joint in composite bridges with integral abutments. Construction and Building Materials, 186, pp. 709-730.
[22] Veljkovic, M. (2007). Project: Economic and Durable Design of Composite Bridges with Integral Abutments.
[23] Mattock, A. H. and Gaafar, G. H. (1982, March). Strength of embedded steel sections as brackets. Journal Proceedings 79(2), pp. 83-93.
[24] Tschemmernegg, F. and Humer, C. (1988). The design of structural steel frames under consideration of the nonlinear behaviour of joints. Journal of Constructional Steel Research, 11(2), pp. 73-103.
[25] Hawkins, N. M. (1970). The bearing strength of concrete for strip loadings. Magazine of concrete research, 22(71), pp. 87-98.